Ultramicroscopy 134 (2013) 160–166

Contents lists available at ScienceDirect

Ultramicroscopy

journal homepage: www.elsevier.com/locate/ultramic

Finite element simulations of electrostatic dopant potentials in thin semiconductor specimens for electron holography

P.K. Somodi [a], A.C. Twitchett-Harrison [a], P.A. Midgley [a], B.E. Kardynał [b], C.H.W. Barnes [c], R.E. Dunin-Borkowski [d,*]

[a] Department of Materials Science and Metallurgy, University of Cambridge, Pembroke Street, Cambridge CB2 3QZ, United Kingdom
[b] Peter Grünberg Institute 9, Forschungszentrum Jülich, D-52425 Jülich, Germany
[c] Department of Physics, University of Cambridge, Madingley Road, Cambridge CB3 0HE, United Kingdom
[d] Ernst Ruska-Centre for Microscopy and Spectroscopy with Electrons and Peter Grünberg Institute 5, Forschungszentrum Jülich, D-52425 Jülich, Germany

ARTICLE INFO

Available online 16 July 2013

Keywords:
Semiconductor *p–n* junction
Dopant potential
Off-axis electron holography
Finite element simulation.

ABSTRACT

Two-dimensional finite element simulations of electrostatic dopant potentials in parallel-sided semiconductor specimens that contain *p–n* junctions are used to assess the effect of the electrical state of the surface of a thin specimen on projected potentials measured using off-axis electron holography in the transmission electron microscope. For a specimen that is constrained to have an equipotential surface, the simulations show that the step in the *projected* potential across a *p–n* junction is always lower than would be predicted from the properties of the bulk device, but is relatively insensitive to the value of the surface state energy, especially for thicker specimens and higher dopant concentrations. The depletion width measured from the projected potential, however, has a complicated dependence on specimen thickness. The results of the simulations are of broader interest for understanding the influence of surfaces and interfaces on electrostatic potentials in nanoscale semiconductor devices.

© 2013 Elsevier B.V. All rights reserved.

1. Introduction

The development of a technique that can be used to characterize electrostatic dopant potentials with nanometer spatial resolution is important for the design and optimization of future generations of semiconductor devices. Off-axis electron holography in the transmission electron microscope (TEM) promises to provide this capability. The technique allows the phase shift ϕ of an electron wave that has passed through an electron-transparent specimen to be measured quantitatively [1,2]. For a non-magnetic specimen, the phase shift can be expressed in the form

$$\phi(x,y) = C_E \int V(x,y,z)\,\mathrm{d}z, \tag{1}$$

where V is the electrostatic potential within and around the specimen, z is the electron beam direction and C_E is a constant that depends on the microscope accelerating voltage. If external electrostatic fringing fields [3–7], electron-beam-induced specimen charging [8–10] and the effects of dynamical diffraction [11,12] can all be neglected, then the value of ϕ at each position across the field of view is directly proportional to the average value of $V(x,y,z)$ in the specimen projected in the electron beam direction z.

The largest contribution to V in a TEM specimen is usually associated with its mean inner potential, V_0, which depends primarily on its composition and density and has an experimentally measured magnitude of ~12 V for Si [13]. Local variations in the species or concentration of dopant atoms rarely change the scattering factor or density of a material strongly enough to affect V_0 directly [14]. However, they result in an additional contribution to V, which is associated with longer-range charge redistribution and is often referred to as the dopant potential [15].

If the specimen thickness is known (and ideally constant across the region of interest) then, in principle, a phase image recorded using off-axis electron holography can be used to measure the dopant potential in a TEM specimen of a semiconductor device quantitatively. However, in practice, the step in the phase shift across a *p–n* junction recorded experimentally using off-axis electron holography is almost always lower than would be expected from the properties of the bulk device [16–19]. This discrepancy is primarily associated with the effects of surface depletion and additional near-surface physical and electrical damage from TEM specimen preparation [20–22]. Both effects are difficult to include in simulations of the potential in a thin specimen, in part because the electrical state of a TEM specimen surface is unknown. Accordingly, here we present finite element simulations that

* Corresponding author. Tel.: +49 2461 619297.
E-mail addresses: rafaldb@gmail.com, rdb@fz-juelich.de (R.E. Dunin-Borkowski).

0304-3991/$ - see front matter © 2013 Elsevier B.V. All rights reserved.
http://dx.doi.org/10.1016/j.ultramic.2013.06.023

illustrate the influence of surface state energy on projected electrostatic potential for a thin, parallel-sided semiconductor specimen that contains a p–n junction [23], including the effects of sub-surface specimen damage and applied reverse bias in the simulations. We use the results to discuss the degree to which quantitative information about the electrical properties of a semiconductor device can be inferred from a phase image recorded using off-axis electron holography.

2. Method

We use finite element simulations, within the Diffpack programming package [24], to iteratively solve the non-linear differential equations that relate the dopant potential to the charge density for a p–n junction in a parallel-sided semiconductor specimen [25]. Only semi-classical equations are used, as quantum confinement effects are insignificant for the devices that are considered here. The simulations require an iterative solution of Poisson's equation (which is used to determine the potential associated with a given charge distribution) and the Thomas Fermi approximation (which is used to determine the charge associated with the potential) until self-consistency is achieved. The equations that are used in the simulations are summarized in the Appendix.

We perform the simulations for a temperature of 273 K using the specimen geometry defined in Fig. 1. As Poisson's equation is second order, two boundary conditions are required to obtain a solution for the potential. The edges of the specimen marked C and D in Fig. 1 are set to have the properties of an isolated semiconductor of bulk p-type or n-type material. In order to define the boundary conditions on the surfaces marked A and B in Fig. 1, we make use of the experimental observation that electrostatic fringing fields are almost never observed outside TEM specimens that contain p–n junctions [16–22]. We constrain the specimen surface to be an equipotential by ensuring that the surface state energy relative to the Fermi level on surfaces A and B takes a single chosen value, typically resulting in Fermi level pinning on the specimen surfaces.

Although the positions of the surface state energies in the band gap are unknown, three distinct situations can occur depending on the value chosen for the surface state energy [25]. In an n-type semiconductor, if surface states occur in the band gap, then they are able to accept electrons from the donor level and the conduction band and a region of positive charge (a surface depletion layer) forms. If the Fermi level decreases below the valence band, then inversion occurs, the surface of the n-type semiconductor becomes

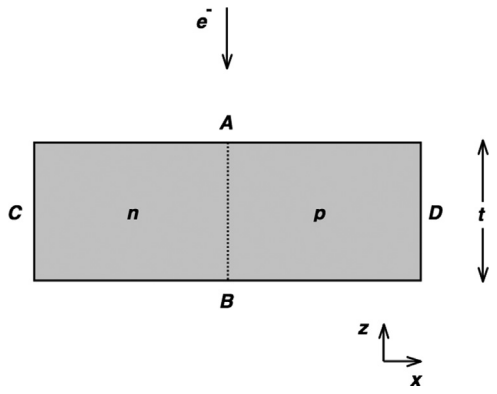

Fig. 1. Schematic diagram showing the direction of the electron beam relative to a parallel-sided TEM specimen of thickness t containing a p–n junction. A and B represent the surface of the thin specimen, which is set to be an equipotential in the simulation. C and D represent the left and right boundaries of the simulation, at which the semiconductor is defined to have the properties of either pure n-type (C) or pure p-type (D) material.

p-like and the Fermi level decreases below that expected for an intrinsic semiconductor. The third situation occurs when the surface states display donor-type characteristics, resulting in the presence of free electrons in the conduction band below the specimen surface.

The finite element simulations described below were each carried out on rectangular grids of 90×30 pixels. The accuracy of the final calculated electrostatic potentials was checked by systematically assessing the effect of changing the sampling density, the number of iterations and the relaxation parameter used [23]. The sign convention for the potential used throughout this paper corresponds to the n-type side of a p–n junction having a lower electrostatic potential than the p-type side, which is consistent with that used by the semiconductor physics community but opposite to that used in most of the electron microscopy literature. It should be noted that the simulations are each intended to illustrate the magnitudes of the separate effects on the potential that are associated with different surface and near-surface conditions, rather than to model the material-dependent situation in a specific TEM specimen fully.

3. Results

3.1. Unbiased clean specimen

Fig. 2 shows representative finite element simulations of electrostatic potentials in parallel-sided Si specimens of thickness 300 nm that each contain a single abrupt symmetrical p–n junction formed from Sb (n-type) and B (p-type) dopants. The material parameters are given in Table 1. The dopant concentrations on both sides of the junction are 10^{19}, 10^{18}, 10^{17} or 10^{16} cm^{-3} and the surface state energy is chosen to be 0.7 eV above the Fermi level on the top and bottom surfaces of the specimen. This is the conduction band energy that has been measured experimentally for a clean Si surface [26]. (This choice of surface state energy is arbitrary, in the absence of a value for the surface of a real TEM specimen, which is always unknown). The simulations shown in Fig. 2 represent the possible distributions of the potential in specimens that have suffered no sub-surface damage due to specimen preparation. They show that simply setting the surface of a specimen to an equipotential can influence the potential deep within it and that this effect is strongest for lower values of dopant concentration and specimen thickness. The details of the asymmetry in the contours between the p and n sides of the junction, which is visible close to the specimen surface, depend on the surface state energy. For a dopant concentration of 10^{16} cm^{-3}, the effects of the specimen surface on the potential are so strong that no part of the specimen retains close-to-bulk-like properties when it has a thickness of 300 nm.

Fig. 3 shows line profiles of the average value of the dopant potential in the specimen, obtained by projecting the simulations shown in Fig. 2 in the electron beam direction. Each line profile represents the information about the potential in the specimen that would be obtained experimentally from a measurement of the phase shift across a p–n junction, combined with an independent knowledge of the specimen thickness. For comparison, one-dimensional simulations (representing the limits of such calculations for very thick specimens) are also shown.

Fig. 4 shows the step in the projected potential across the position of the p–n junction, measured from the profiles shown in Fig. 3 and plotted as a function of both surface state energy (Fig. 4a) and specimen thickness (Fig. 4b). Fig. 4a shows that the step in the projected potential is approximately insensitive to surface state energy, especially for higher dopant concentrations, whether or not this energy lies within the band gap of the bulk

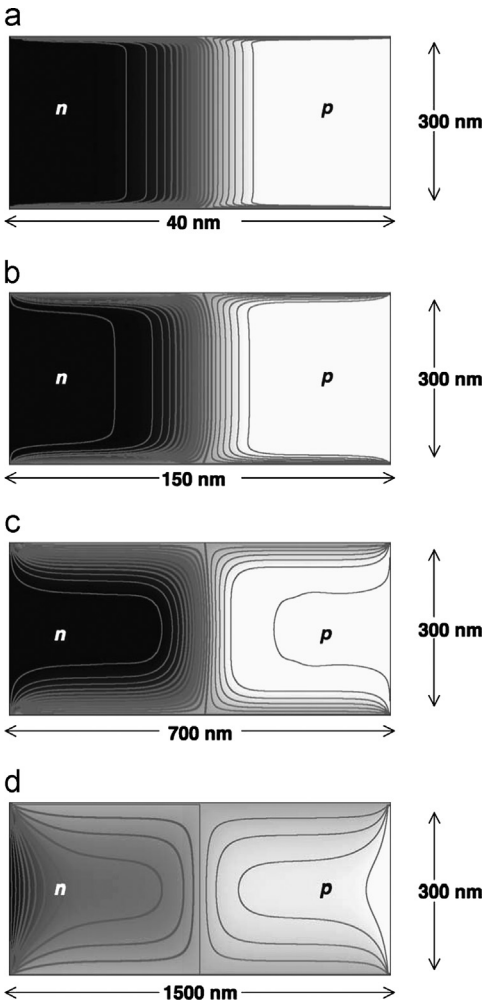

Fig. 2. Finite element simulations of electrostatic potential in parallel-sided specimens of thickness 300 nm containing abrupt symmetrical Si p–n junctions formed from (a) 10^{19}, (b) 10^{18}, (c)10^{17} and (d) 10^{16} cm^{-3} of Sb (n-type) and B (p-type) dopants. The surface state energy at edges A and B marked in Fig. 1 is set to 0.7 eV above the Fermi level. Contours of spacing 0.05 V are shown. For visual reasons, the horizontal scale is set to be different in each figure, in order to show the variation in potential close to the position of the junction.

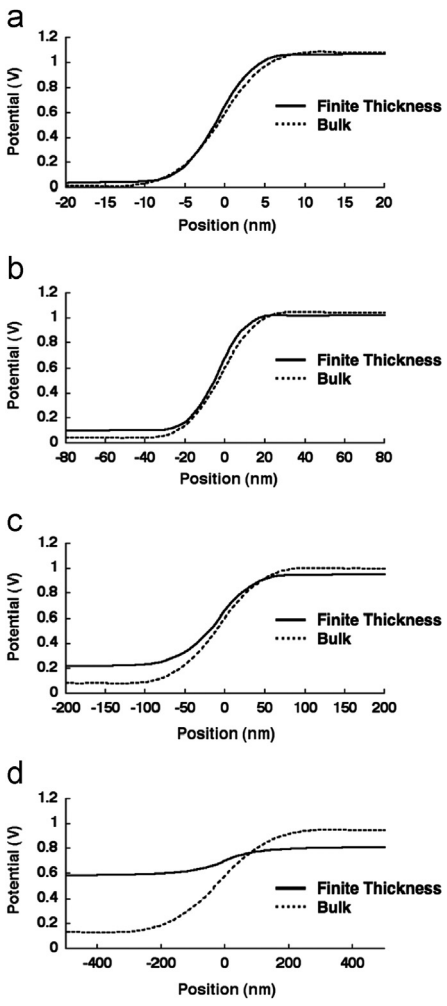

Fig. 3. Projected potential averaged through the thickness of the specimen in a direction perpendicular to its surface, determined from the two-dimensional simulations shown in Fig. 2. The dopant concentrations are (a) 10^{19}, (b) 10^{18}, (c) 10^{17} and (d) 10^{16} cm^{-3}. The dashed lines show one-dimensional finite element simulations calculated for bulk-like material (i.e., in the limit of a very thick specimen). The sign convention used here, which is consistent with that used in the semiconductor physics literature but opposite to that used in most electron microscopy papers, corresponds to the n-type side of a p–n junction having a lower electrostatic potential than the p-type side.

Table 1
Material-dependent parameters for Si used in the present simulations [25]. m_0 is the rest mass of an electron. The energy of the donor atoms is given relative to the conduction band. The energy of the acceptor atoms is given relative to the valence band.

Effective electron mass (m_0)	Effective hole mass (m_0)	Band gap (eV)	Donor	Donor energy (eV)	Acceptor	Acceptor energy (eV)
0.26	0.69	1.12	Sb	0.039	B	0.045

material (Fig. 4a). For lower dopant concentrations, this insensitivity to surface state energy is also expected to hold for significantly greater specimen thicknesses. Fig. 4b confirms that the step in the projected potential tends to the bulk-like value as the specimen thickness increases and that it is reduced most strongly from this value when either the specimen thickness or the dopant concentration is low. For a Si specimen of thickness 300 nm, as a result of surface depletion alone, the step in potential that would be inferred from a measured phase image is approximately 97, 92, 80 and 35% of that expected for a bulk-like device for dopant concentrations of 10^{19}, 10^{18}, 10^{17} and 10^{16} cm^{-3}, respectively.

Fig. 5 shows the depletion width measured from the projected potential profiles in Fig. 3, plotted as a function of surface state energy. Surprisingly, the measured depletion width across the p–n junction measured from the projected potential is smaller and not larger than the bulk-like value at low specimen thicknesses, before rising above it and finally tending towards it asymptotically at large thicknesses. This behavior results from the fact that the surface charge density has the same sign as that at the junction (i.e., positive in the n-type region and negative in the p-type region). The charge that builds up at the specimen surface therefore repels the charge at the junction, reducing the depletion width. As the specimen thickness increases, the surface influences a smaller proportion of the specimen. Just as for the step in projected potential, the measured depletion width is affected little by surface state energy, especially for higher dopant concentrations and specimen thicknesses. Taken together, the graphs in Figs. 4 and 5 suggest that, for dopant concentrations below approximately 10^{16} cm^{-3}, measurements of the electron holographic phase shift across a Si p–n junction are always likely to be difficult for specimen thicknesses of below 500 nm.

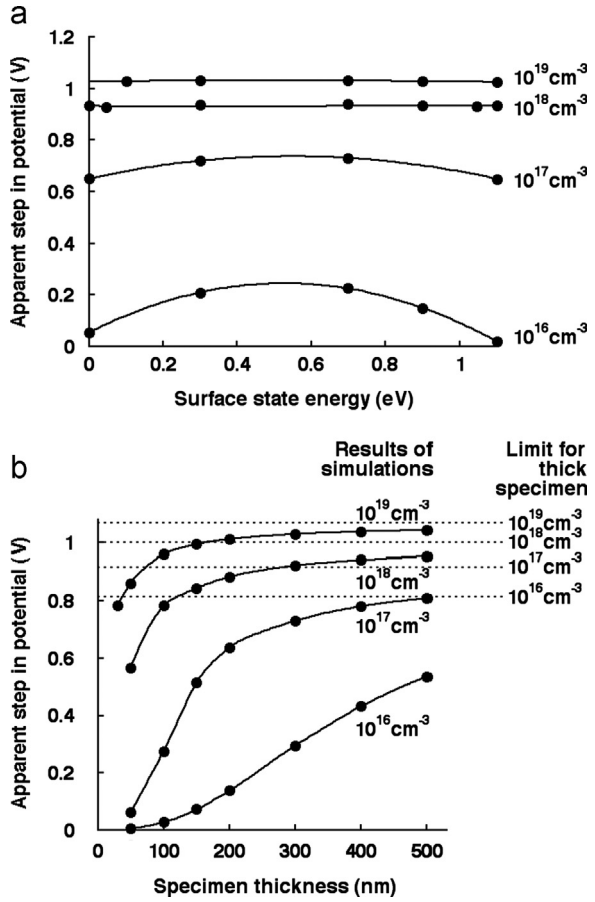

Fig. 4. (a) Apparent step in potential across an abrupt symmetrical Si p–n junction that would be measured from a projected potential profile, similar to those shown in Fig. 3, plotted as a function of surface state energy (relative to the Fermi level) for a specimen of thickness 300 nm for dopant concentrations of 10^{19}, 10^{18}, 10^{17} and 10^{16} cm^{-3}. (b) Apparent step in potential plotted as a function of specimen thickness for the dopant concentrations indicated, calculated for a surface state energy of 0.7 eV above the Fermi level. Limiting values for a very thick specimen (1.07, 1.00, 0.92 and 0.82 V for dopant concentrations of 10^{19}, 10^{18}, 10^{17} and 10^{16} cm^{-3}, respectively), determined using one-dimensional finite element simulations, are shown using dashed lines.

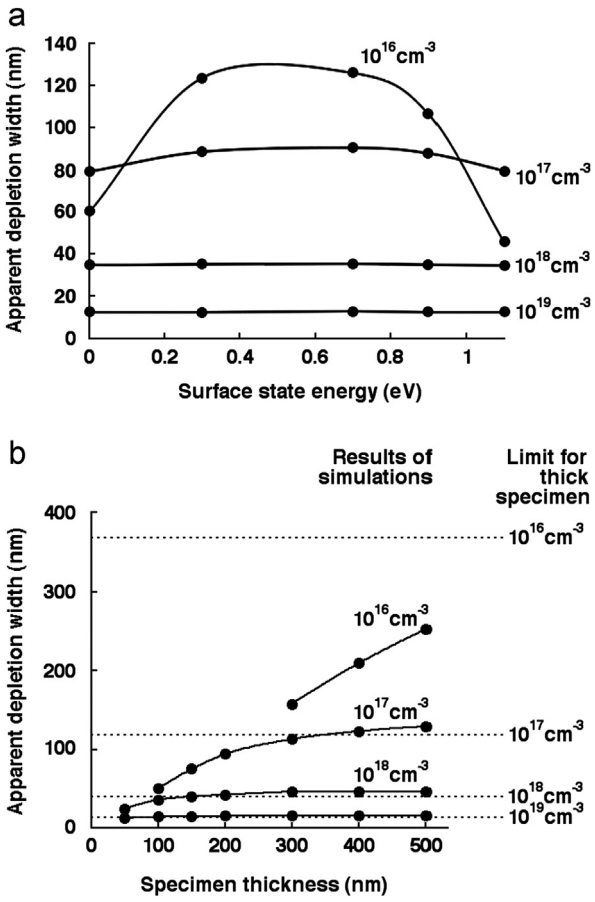

Fig. 5. (a) Apparent depletion width across an abrupt symmetrical Si p–n junction that would be measured from a projected potential profile, similar to those shown in Fig. 3, plotted as a function of surface state energy (relative to the Fermi level) for a specimen of thickness 300 nm for dopant concentrations of 10^{19}, 10^{18}, 10^{17} and 10^{16} cm^{-3}. (b) Apparent depletion width plotted as a function of specimen thickness for the dopant concentrations indicated, calculated for a surface state energy of 0.7 eV above the Fermi level. Limiting values for a very thick specimen (14, 42, 122 and 377 nm for dopant concentrations of 10^{19}, 10^{18}, 10^{17} and 10^{16} cm^{-3}, respectively), determined using one-dimensional finite element simulations, are shown using dashed lines. In each graph, the apparent depletion width is defined as the distance over which the charge density is non-zero, on the assumption that the total charge determined from the projected potential profile is redistributed in the depletion region of an abrupt p–n junction in which the charge density is either equal to the dopant concentration or zero.

Similar behavior to that shown in Fig. 2 has been observed experimentally using electron holographic tomography [27]. However, additional factors such as near-surface defects and electron-beam-induced electron–hole pair generation were then also likely to be significant (see below).

3.2. Sub-surface effects

We used two alternative approaches to assess the effects of specimen preparation for electron microscopy on electrostatic dopant potentials in thin TEM specimens.

Model 1 assumes a decrease in dopant activation close to the specimen surface, as might be expected from the presence of defects such as vacancies or self-interstitials [28–30], whose electronic energy levels lie in the forbidden energy band of the specimen and can be thought of, to a first approximation, as effectively reducing the free charge carrier concentration. We model these effects, to a first approximation, by specifying a reduced dopant concentration of 10^{15}, 10^{16} or 10^{17} cm^{-3} on both sides of the p–n junction in a layer of thickness 10, 20, 30 or 40 nm just below the specimen surface. Fig. 6 shows examples of the resulting simulations for a Si specimen of thickness 270 nm containing 3×10^{18} cm^{-3} of Sb in the n-type region and 4×10^{18} cm^{-3} of B in the p-type region, with the surface state energy again set to 0.7 eV above the Fermi level. In Fig. 6, the effect of the surface layer has moved the apparent position of the junction at the specimen surface, decreasing the potential step and increasing the depletion width. Measurements of the apparent step in potential across the junction, which were obtained from projected potential profiles generated from the simulations shown in Fig. 6 and are plotted as a function of surface layer thickness in Fig. 7, take values of 0.81, 0.85 and 0.87 V for specimen thicknesses of 220, 270 and 410 nm, respectively, when the surface layer has a dopant concentration of 10^{15} cm^{-3} and a thickness of 40 nm. The situation described in model 1, involving an identical reduction in free charge carrier concentration on both sides of the p–n junction, is clearly a simplification of the true situation. In practice, an asymmetric change in free charge carrier concentration across the junction may arise near the specimen surface, possibly resulting in inversion on one side of the junction, depending on the density of defect states and the dopant concentration.

Model 2, in contrast, assumes an increase in p-type doping close to the specimen surface, as might be expected from the use of a technique such as focused ion beam (FIB) milling with Ga ions

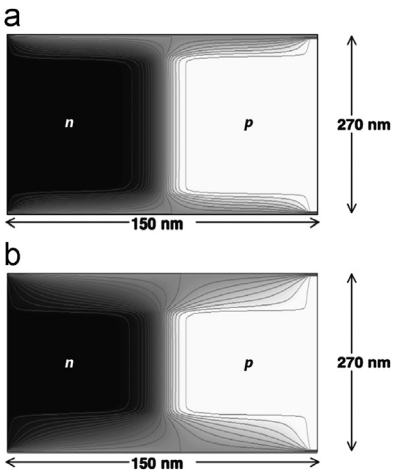

Fig. 6. Finite element simulations of the electrostatic potential in a parallel-sided specimen of thickness 270 nm containing an abrupt Si *p*–*n* junction formed from 3×10^{18} cm^{-3} of Sb (*n*-type) and 4×10^{18} cm^{-3} of B (*p*-type) dopants. The surface state energy at edges *A* and *B* marked in Fig. 1 is set to 0.7 eV above the Fermi level. The free charge carrier concentration close to the specimen surface was modified to represent the effects of TEM specimen preparation, according to model 1 described in the text, by introducing *p*- and *n*-type surface layers of thickness (a) 20 nm and (b) 40 nm that have greatly reduced dopant concentrations of 10^{15} cm^{-3}. Contours of spacing 0.05 V are shown.

[31–36], which introduces *p*-type dopants in Si. Here, we introduce additional *p*-type doping in a surface layer that has a thickness of between 10 and 40 nm, for the same specimens that were considered in Fig. 6. Fig. 8 shows the resulting simulations. Just as in Fig. 6, the introduction of the surface layer moves the apparent position of the junction and increases the depletion width in the surface layer.

For the dopant concentrations considered in Figs. 6–8, both models for the effects of specimen preparation influence the potential in the specimen primarily within the thickness of the damaged or doped surface layer. In this layer, the potential distribution is affected significantly from that expected for an undamaged specimen, as observed experimentally using electron holographic tomography [37,38]. Experimentally, the thickness of the electrically modified surface layer is unknown, even if its physical extent can be characterized in the TEM, and modifications to the potential in the specimen may depend sensitively on the difference between the effective dopant concentration in the surface layer and that in the bulk device, especially if the original dopant concentration is low.

3.3. Reverse bias

In order to model the electrostatic potential in a reverse biased TEM specimen, finite element simulations illustrating the influence of surface state energy were performed by using a logistic function to represent the variation in Fermi level across the junction [23]. Effects associated with carrier injection are beyond the scope of the present manuscript and were not included.

Values obtained from projected potential profiles determined from the simulations are shown in Fig. 9 for a Si specimen of thickness 300 nm doped with 10^{19} cm^{-3} of Sb in the *n*-type region and 10^{19} cm^{-3} of B in the *p*-type region. As expected, the depletion

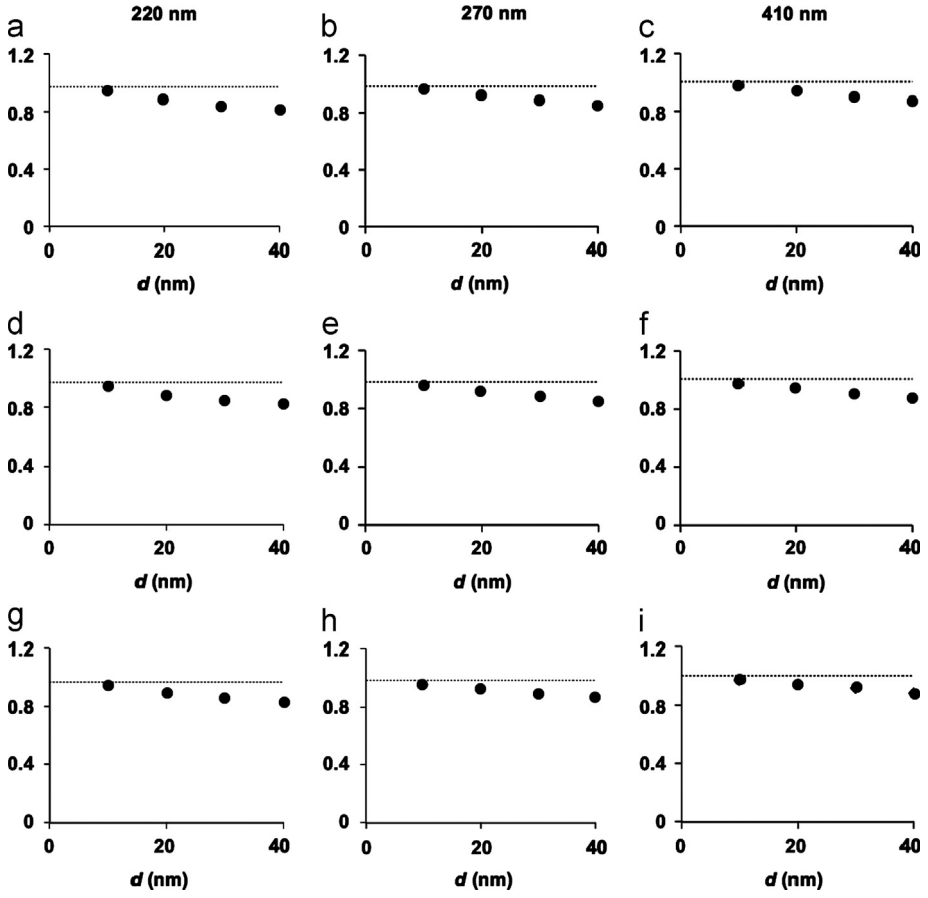

Fig. 7. Apparent step in potential in V across Si *p*–*n* junctions similar to those shown in Fig. 6, plotted as a function of surface layer thickness *d*. The dopant concentrations in the surface layers are (a)–(c) 10^{15} cm^{-3}; (d)–(f) 10^{16} cm^{-3} and (g)–(i) 10^{17} cm^{-3}. The dashed lines show the apparent steps in potential when $d=0$, i.e., for no surface layers.

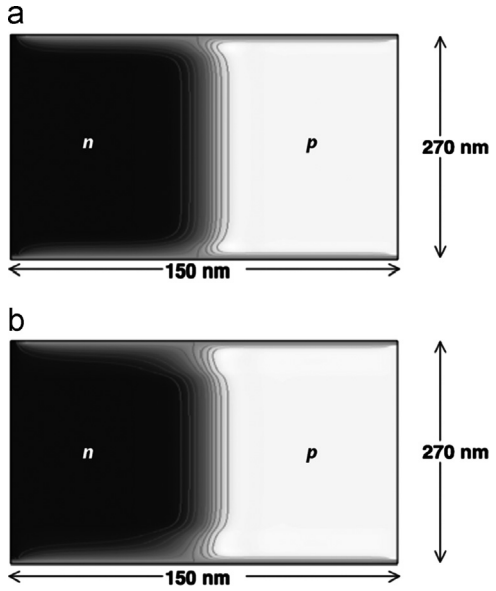

Fig. 8. Finite element simulations of the electrostatic potential in a parallel-sided specimen of thickness 270 nm containing an abrupt Si *p*–*n* junction formed from 3×10^{18} cm^{-3} of Sb (*n*-type) and 4×10^{18} cm^{-3} of B (*p*-type) dopants. The surface state energy at edges *A* and *B* marked in Fig. 1 is set to 0.7 eV above the Fermi level. The dopant concentration close to the specimen surface was modified to represent the effects of TEM specimen preparation, according to Model 2 described in the text, by including additional *p*-type dopants into a layer of thickness (a) 20 and (b) 40 nm just below the specimen surface. The resulting modified dopant concentrations in the surface layers are 1×10^{18} cm^{-3} in the *n*-type region and 6×10^{18} cm^{-3} in the *p*-type region. Contours of spacing 0.05 V are shown.

width measured from the projected potential profiles is found to increase approximately in proportion to the square root of the applied reverse bias. Just as for the unbiased specimen, the presence of the specimen surfaces is found to reduce the measured step in potential across the junction and to increase the measured depletion width, with little sensitivity to surface state energy. However, the slopes of the graphs of depletion width plotted as a function of reverse bias are different between one-dimensional (bulk-like) and full two-dimensional simulations, indicating that the effect of the specimen surfaces on the potential changes with applied reverse bias and cannot be inferred simply from simulations of potentials in unbiased specimens.

4. Discussion and Conclusions

We have used finite element simulations to show that, simply by setting the surface of a TEM specimen that contains a *p*–*n* junction to be an electrostatic equipotential, the potential can be affected substantially deep within the specimen, especially for lower dopant concentrations and specimen thicknesses. Such surface effects are highly dependent on dopant concentration. The step in potential across a *p*–*n* junction measured from a projected potential profile is always reduced when compared with the value expected for a bulk-like specimen. This effect is greatest for thinner specimens and lower dopant concentrations. For higher dopant concentrations and thicker specimens, the step in potential and depletion width are only weakly dependent on surface state energy. For a Si specimen of thickness 300 nm with a dopant concentration of 10^{16} cm^{-3}, no part of the specimen has close-to-bulk-like properties, even at its center. It is therefore surprising that experimental results in the literature report both the successful application of electron holography to the characterization of a *p*–*n* junction in Si with a dopant concentration of only 10^{15} cm^{-3} [39] and quantitative agreement between measured steps in potential across *p*–*n* junctions and those expected in bulk-like

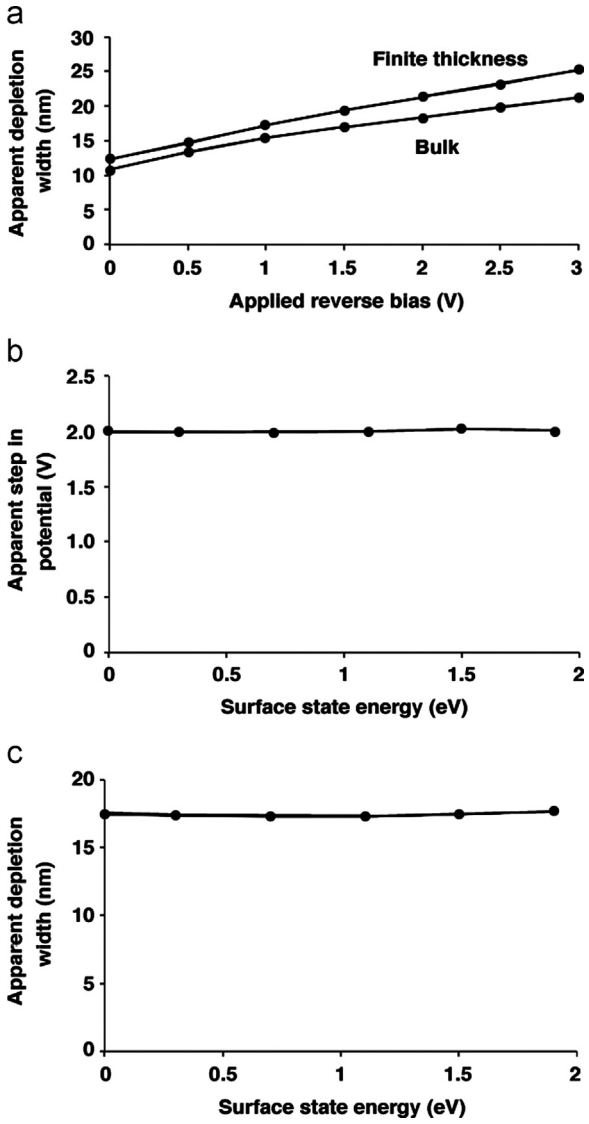

Fig. 9. (a) Depletion width across a reverse biased Si *p*–*n* junction, determined from finite element simulations for a specimen doped with 10^{19} cm^{-3} of Sb in the *n*-type region and 10^{19} cm^{-3} of B in the *p*-type region and plotted as a function of applied reverse bias for a surface state energy of 0.7 eV relative to the Fermi level in the *n*-type region far from the junction. The depletion widths are measured from both one-dimensional (bulk-like) potential profiles (lower curve) and projected potential profiles determined from two-dimensional simulations for a specimen of thickness 300 nm (upper curve). Projected potential profiles determined from the two-dimensional simulations were used to measure values for the apparent step in potential of 2.87, 2.41, 1.95, 1.48 and 1.00 V and for the apparent depletion width of 45, 41, 36, 31 and 26 nm for applied reverse bias voltages of 0.0, 0.5, 1.0, 1.5 and 2.0 V, respectively. (b) Apparent step in potential and (c) apparent depletion width across a reverse biased Si *p*–*n* junction, measured from projected potential profiles determined from two-dimensional finite element simulations for a specimen of thickness 300 nm and a reverse bias voltage of 1 V. The measured values are plotted as a function of surface state energy relative to the Fermi level in the *n*-type region far from the junction.

devices [40]. These observations may result from errors in measurements of specimen thickness, as they are not expected to result from the presence of oxide layers on the specimen surfaces [41,42].

Most experimental electron holography studies have reported lower steps in potential across *p*–*n* junctions than bulk-like values, in agreement with our calculations. However, the steps in potential that are measured experimentally are often much lower than those described here and the depletion widths significantly larger, suggesting that the effects of specimen preparation (and electron beam illumination) on the electrical properties of TEM specimens

can be much more severe than we have considered here. The reverse bias that is applied experimentally across a p–n junction in a TEM specimen may also be lower than that intended as a result of the presence of current paths associated with series or parallel resistance in other parts of the TEM specimen [9], as well as due to junction breakdown. The present simulations could be extended in the future by including continuity equations to model electron–hole pair generation and specimen currents.

Fortunately, if the dopant concentration is high (as in many modern devices), our simulations show that the effect of specimen surfaces on the measured potential is small for large specimen thicknesses. The step in the projected potential across a p–n junction is then also relatively insensitive to surface state energy.

The broader importance of our simulations is emphasized by the need to design and characterize the increasingly three-dimensional nature of semiconductor devices, in which doped regions can be located close to surfaces or interfaces that may affect their electrical properties [43,44].

Acknowledgments

We are grateful to D. Cooper, G. Pozzi, W.O. Saxton and S. Rahman for discussions. Financial support is gratefully acknowledged from the EPSRC, the Royal Society, Newnham College, Cambridge and the European Research Council.

Appendix

The total charge density in the semiconductor device is assumed to take the form

$$\rho = e\,(N_d - N_a - n_c - n_d + p_v + p_a) \tag{A1}$$

where N_d is the density of donor atoms, N_a is the density of acceptor atoms, n_c is the density of electrons in the conduction band, n_d is the density of electrons in the donor levels, p_v is the density of holes in the valence band, and p_a is the density of holes in the acceptor levels.

The concentrations of the donor and acceptor atoms are used as parameters in the simulations and the values of the other quantities are determined from the following equations

$$n_c = 2\left(\frac{m_e kT}{2\pi\hbar^2}\right)^{\frac{3}{2}} \exp\left(\frac{E_f - E_c}{kT}\right) \tag{A2}$$

$$p_v = 2\left(\frac{m_h kT}{2\pi\hbar^2}\right)^{\frac{3}{2}} \exp\left(\frac{E_v - E_f}{kT}\right) \tag{A3}$$

$$n_d = N_d \frac{2}{1 + 2\exp\left(\frac{E_d - E_f}{kT}\right)} \tag{A4}$$

$$p_a = N_a \frac{2}{1 + 2\exp\left(\frac{E_f - E_a}{kT}\right)} \tag{A5}$$

where E_f is the Fermi energy, E_c is the conduction band energy, E_v is the valence band energy, E_a is the energy of the acceptor level, and E_d is the energy of the donor level.

The charge density is related to the electrostatic potential using Poisson's equation

$$\nabla^2 V = -\frac{\rho}{\varepsilon}, \tag{A6}$$

where ε is the permittivity of the material and $V = -E_c/e$.

As the band edge profiles $E_c(x,y,z)$ and $E_v(x,y,z)$ depend on the charge density distribution $\rho(x,y,z)$, for each simulation the set of coupled equations A1 to A6 was solved iteratively using a finite element calculation until self-consistent band profiles and charge densities were found.

References

[1] R.E. Dunin-Borkowski, M.R. McCartney, D.J. Smith, Encyclopaedia of Nanoscience and Nanotechnology, in: H.S. Nalwa (Ed.), American Scientific Publishers, Stevenson Ranch, 2004, pp. 41–100.
[2] Introduction to Electron Holography. In: Völkl, E., Allard, L.F., Joy, D.C., (Eds.) Kluwer Academic/Plenum Publishers, New York, 1998.
[3] R.E. Dunin-Borkowski, W.O. Saxton, Acta Crystallographica A 53 (1997) 242–250.
[4] R.E. Dunin-Borkowski, Ultramicroscopy 83 (2000) 193–216.
[5] A.C. Twitchett, R.E. Dunin-Borkowski, P.A. Midgley, Physical Review Letters 88 (2002) 238302.
[6] M. Beleggia, P.F. Fazzini, G. Pozzi, Ultramicroscopy 96 (2003) 93–103.
[7] S. von Alfthan, N.A. Benedek, L. Chen, A. Chua, D.J.H. Cockayne, K.J. Dudeck, C. Elsässer, M.W. Finnis, C.T. Koch, B. Rahmati, M. Rühle, S.-J. Shih, A.P. Sutton, Annual Review of Materials Research 40 (2010) 557–599.
[8] L. Houben, M. Luysberg, T. Brammer, Physical Review B 70 (2004) 165313.
[9] D. Cooper, R. Truche, A.C. Twitchett-Harrison, P.A. Midgley, R.E. Dunin-Borkowski, Journal of Microscopy 233 (2009) 102–113.
[10] D. Cooper, A.C. Twitchett-Harrison, P.A. Midgley, R.E. Dunin-Borkowski, Journal of Applied Physics 101 (2007) 094508.
[11] M. Gajdardziska-Josifovska, M.R. McCartney, W.J. de Ruijter, D.J. Smith, J. K. Weiss, J.M. Zuo, Ultramicroscopy 50 (1993) 285–299.
[12] A. Lubk, D. Wolf, H. Lichte, Ultramicroscopy 110 (2010) 438–446.
[13] P. Formanek, M. Kittler, Solid State Phenomena 108–109 (2005) 603–608.
[14] D. Cooper, R.E. Dunin-Borkowski, Microscopy, 62 suppl. 1, 2013, S87-S98. 〈http://dx.doi.org/10.1093/jmicro/dft014〉.
[15] W.D. Rau, P. Schwander, F.H. Baumann, W. Höppner, A. Ourmazd., Physical Review Letters 82 (1999) 2614.
[16] A.C. Twitchett, R.E. Dunin-Borkowski, R.F. Broom, P.A. Midgley, Journal of Physics: Condensed Matter 16 (2004) S181–S192.
[17] A.C. Twitchett, R.E. Dunin-Borkowski, R.J. Hallifax, R.F. Broom, P.A. Midgley, Journal of Microscopy 214 (2004) 287–296.
[18] A.C. Twitchett, R.E. Dunin-Borkowski, R.J. Hallifax, R.F. Broom, P.A. Midgley, Microscopy and Microanalysis 11 (2005) 66–78.
[19] A.C. Twitchett, R.E. Dunin-Borkowski, P.A. Midgley, Philosophical Magazine A 86 (2006) 5805–5823.
[20] D. Cooper, C. Ailliot, J.-P. Barnes, J.-M. Hartmann, P. Salles, G. Benassayag, R.E. Dunin-Borkowski, Ultramicroscopy 110 (2010) 383–389.
[21] D. Cooper, P. Rivallin, J.-M. Hartmann, A. Chabli, R.E. Dunin-Borkowski, Journal of Applied Physics 106 (2009) 064506.
[22] D. Cooper, A.C. Twitchett, P.K. Somodi, P.A. Midgley, R.E. Dunin-Borkowski, I. Farrer, D.A. Ritchie, Applied Physics Letters 88 (2006) 063510.
[23] P.K. Somodi, Ph.D. dissertation, University of Cambridge, 2006.
[24] H.P. Langtangen, Computational Partial Difference Equations, Springer, 2003.
[25] S.M. Sze, Semiconductor Devices: Physics and Technology, 2nd edition, Wiley, 2002.
[26] H. Lüth, Solid Surfaces Interfaces and Thin Films, 4th edition, Springer, 2001.
[27] D. Wolf, A. Lubk, H. Lichte, H. Friedrich, Ultramicroscopy 110 (2010) 390–399.
[28] H. Seong, L.J. Lewis, Physical Review B 53 (1996) 9791–9796.
[29] E.G. Song, E. Kim, Y.H. Lee, Y.G. Hwang, Physical Review B 48 (1993) 1486–1489.
[30] B.G. Svensson, B. Mohadjeri, A. Hallén, J.H. Svensson, J.W. Corbett, Physical Review B 43 (1991) 2292–2298.
[31] R.M. Langford, A.K. Petford-Long, Journal of Vacuum Science and Technology A 19 (2001) 2186–2193.
[32] S. Rubanov, P.R. Munroe, Journal of Microscopy 214 (2004) 213–221.
[33] T. Ishitani, H. Koike, T. Yaguchi, T. Kamino, Journal of Vacuum Science and Technology B 16 (1998) 1907–1913.
[34] R.E. Dunin-Borkowski, S.B. Newcomb, T. Kasama, M.R. McCartney, M. Weyland, P.A. Midgley, Ultramicroscopy 103 (2005) 67–81.
[35] Z. Wang, T. Hirayama, K. Sasaki, H. Saka, N. Kato, Applied Physics Letters 80 (2002) 246–248.
[36] Z. Wang, T. Kato, T. Hirayama, K. Sasaki, H. Saka, N. Kato, Journal of Vacuum Science and Technology B 21 (2003) 2155–2188.
[37] A.C. Twitchett, T.J.V. Yates, S.B. Newcomb, R.E. Dunin-Borkowski, P.A. Midgley, Nano Letters 7 (2007) 2020–2023.
[38] A.C. Twitchett-Harrison, T.J.V. Yates, R.E. Dunin-Borkowski, P.A. Midgley, Ultramicroscopy 108 (2008) 1401–1407.
[39] Z. Wang, T. Kato, N. Shibata, T. Hirayama, N. Kato, K. Sasaki, H. Saka, Applied Physics Letters 81 (2002) 478–480.
[40] M.A. Gribelyuk, M.R. McCartney, J. Li, C.S. Murthy, P. Ronsheim, B. Doris, J.S. McMurray, S. Hegde, D.J. Smith, Physical Review Letters 89 (2002) 025502.
[41] M. Beleggia, P.F. Fazzini, P.G. Merli, G. Pozzi, Physical Review B 67 (2003) 045328.
[42] P.F. Fazzini, P.G. Merli, G. Pozzi, F. Ubaldi, Physical Review B 72 (2005) 085312.
[43] P.S. Chakraborty, M.R. McCartney, J. Li, C. Gopalan, U. Singisetti, S.M. Goodnick, T.J. Thornton, M.N. Kozicki, Physica E 19 (2003) 161–172.
[44] P.S. Chakraborty, M.R. McCartney, J. Li, C. Gopalan, M. Gilbert, S.M. Goodnick, T.J. Thornton, M.N. Kozicki, IEEE Transactions on Nanotechnology 2 (2003) 102–109.